Effects of vernal equinox solar eclipse on temperature and wind direction in Switzerland

Werner Eugster[1], Carmen Emmel[1], Sebastian Wolf[2], Nina Buchmann[1], Joseph P. McFadden[3], and C. David Whiteman[4]

[1]ETH Zurich, Department of Environmental Systems Science, Institute of Agricultural Sciences, 8092 Zurich, Switzerland
[2]ETH Zurich, Department of Environmental Systems Science, Institute of Terrestrial Ecosystems, 8092 Zurich, Switzerland
[3]University of California, Santa Barbara, Department of Geography, Earth Research Institute, Santa Barbara, California, 93106–4060, USA
[4]University of Utah, Atmospheric Sciences Department, Salt Lake City, Utah, USA

Correspondence to: W. Eugster (eugsterw@ethz.ch)

Abstract. The vernal equinox total solar eclipse of 20 March 2015 produced a maximum occultation of 65.8 to 70.1% over Switzerland during the morning hours (09:22 to 11:48 CET). Skies were generally clear over the Swiss Alps due to a persistent high-pressure band between the UK and Russia associated with a rather weak pressure gradient over the continent. To assess the effects of penumbral shading on near-surface meteorology across Switzerland, air temperature data measured at 10-minute intervals at 184 MeteoSwiss weather stations that reported air temperature at 10-minute intervals were used. Wind speed and direction data were available from 165 of these stations. Additionally, six Swiss FluxNet eddy covariance flux (ECF) sites provided turbulent measurements at 20 Hz resolution.

During maximum occultation the temperature drop was up to 5.8 K at a mountain site where cold air can pool in a topographic depression. The bootstrapped average of the maximum temperature drops of all 184 MeteoSwiss sites during the solar eclipse was 1.51 ± 0.02 K (mean $\pm$ SE). A detailed comparison with literature values since 1834 showed a temperature decrease by 2.6 ± 1.7 K (average of all reports), with extreme values up to 11 K. On fair weather days under weak larger scale pressure gradients, local thermo-topographic wind systems develop that are driven by small-scale pressure and temperature gradients. At one ECF site, the penumbral shading delayed the morning transition from down-valley to up-valley wind conditions. At another site, it prevented this transition from occurring at all. Data from the 165 MeteoSwiss sites measuring wind direction did not show a consistent pattern of wind direction response to the passing of the penumbral shadow. These results suggest that the local topographic setting had an important influence on the temperature drop and the wind flow patterns during the eclipse. A significant cyclonic effect of the passing penumbral shadow was found in the elevation range ≈1700–2700 m a.s.l., but not at lower elevations of the Swiss Plateau. This contrasts with an earlier theory that the anticyclonic outflow should reach as far as ≈2400 km from the center of the eclipse, which would have included all of Switzerland during the 2015 eclipse. Thus, measurable effects of penumbral shading on the local wind system could be even found at ≈2000 km from the path of the eclipse (that is, Switzerland during the 2015 eclipse), and our results tend to lend support to a newer theory that the anticyclonic cold-air outflow from the center of the eclipse only extends ≈1600 km outwards, with cyclonic flow beyond that distance.

1 Introduction

Solar eclipses have long fascinated scientists and brought about essential scientific knowledge on the meteorologial effects of the phenomenon. The most commonly studied effect is that on temperature at Earth's surface (Table 1, Aplin et al., 2016). Less, however, is known about the effects on local and larger scale wind directions at places where only partial occultation is observed. Here we test the hypothesis that even a partial occultation of a solar eclipse may have short-term influences on wind directions. During a solar eclipse, the new moon passes in front of the sun's disk and thus reduces incoming solar radiation. This astronomic event is typically described with four phases. It begins with the first contact between the moon and the sun as seen by an observer on the Earth. With the first contact, the penumbral shading begins, that is the partial shading where sun rays from one part of the sun's disk are blocked by the moon, whereas sun rays from the opposite side of the sun's disk still reach the observer. This phase ends with the second contact when the moon completely obscures the sun and the observer is in the dark shadow of the moon. During this second phase of totality, only diffuse sunlight reaches Earth's surface. This phase ends with the maximum occultation, when the solar corona can be seen in the case of a total eclipse. With annular and partial eclipses, the maximum occultation simply means the darkest conditions. After the maximum, light levels increase again until the third contact, when the transition from the umbral shadow to the less dark penumbral shadow takes place. The astronomical event ends with the fourth contact, after which meteorological conditions should no longer depend on the moon's position. The second and third contacts are observed only in the narrow band of the umbra during annular or total eclipses.

During the total vernal equinox eclipse of 20 March 2015 (Saros 120, https://eclipse.gsfc.nasa.gov/5MCSE/5MCSE-Maps-10.pdf), which produced a partial occultation over the Swiss Alps, the weather conditions were excellent with mostly clear skies due to a persistent high-pressure band between the UK and Russia, with a rather weak pressure gradient over the continent (MeteoSwiss, 2015). On normal days under weak larger scale pressure gradients, local thermo-topographic wind systems develop that are driven by small-scale pressure and temperature gradients, which are strongest in mountainous areas such as the Swiss Alps. It could hence be expected that during penumbral shading, these thermo-topographic winds would be subject to modifications superimposed by the larger scale circulation generated around the umbra of the solar eclipse. The meteorological conditions during an eclipse are expected to be the same as that of a "cyclone with a cold centre" as described by Ferrel (1890, pp. 337–342). In such a cyclone, the vertical motion is reversed as compared to a typical warm centered cyclone. This leads to a (narrow) core with cyclonic rotation in the cold center of the cyclone and an anticyclonic counterflow around this core. Because of its reversed structure, the cyclonic rotation in a cold-centered cyclone according to Ferrel (1890) is strongest in the upper troposphere and weakest near the surface, whereas the anticyclonic rotation is weakest in the upper troposphere and strongest near Earth's surface.

Based on Ferrel's (1890) concept, Clayton (1901) empirically determined the direct influence of the occultation on wind direction within the shaded area during the 28 May 1900 total eclipse (Saros 126). According to Clayton's (1901) theory, the cyclonic rotation in the center of the umbra is not detectable, but an anticyclonic outflow should be generated in the inner zone of the penumbral shadow. This zone with anticyclonic rotation is expected to extend at least 2400–3200 km (1500 to 2000 miles; Clayton, 1901) from the center of the umbra. In contrast, the outer part of the penumbra is subject to a cyclonic wind

direction rotation (a further ≈1600 km; Fig. 1a). Although Clayton (1901) concluded that this rotational pattern "confirms so well Ferrel's theory of the cold-air cyclone", he did not provide an estimate of the dimension or strength of the cold-air cyclone in the center of the umbra because no cyclonic effects could be seen in his analyses. Following Clayton (1901), Aplin and Harrison (2003) carefully assessed the penumbral winds at Reading and Camborne (UK) during the 11 August 1999 total eclipse (Saros 145) of which a maximum occultation of 97% was observed at Reading. Their 1 Hz ultrasonic anemometer wind speed and wind direction measurements showed a pronounced drop in wind speed during the eclipse. The wind then changed in a cyclonic direction on first contact, and later returned via an anticyclonic rotation to the synoptic wind direction after maximum occultation. Thus, their finding conformed to what is expected for the inner core around the umbra, where Clayton (1901) expected the cold-air cyclone, but did not find it in his own analysis of synoptic-scale weather maps. Aplin and Harrison (2003) thus postulated a revised model with an inner cold core of ca. 160 km around the center of the umbra containing cyclonic flow (Fig. 1b). They expected an anticyclonic rotation outside this zone that extends to ca. 1600 km (1000 mi), with a further outermost zone of cyclonic rotation then extending up to ca. 4800 km (3000 mi).

Bilham (1921) was the first to empirically confirm an indirect effect of the cooling during occultation on wind direction. He reported that "the wind showed a marked tendency to back" (as expected from cyclonic influence of the thermal wind), consistent with the cold-core cyclone in the umbral zone. There is observational evidence of thermal wind effects superimposed on near-surface winds during occultation, but no regional-scale weather prediction model has been able to reproduce this effect successfully. Prenosil (2000) simulated the 11 August 1999 eclipse in Central Europe using a hydrostatic regional weather prediction model. This model was able to produce a slight cyclonic circulation in the surface winds, but it only lasted for some minutes and thus challenges the idea that such a weak effect can be observed in field measurements.

During the vernal equinox eclipse of 2015, we expected a clear difference in wind direction for the Swiss Alps dependent on the Clayton (1901) or the Aplin and Harrison (2003) theories. Thus, we investigated whether the onset of penumbral shading leads to an anticyclonic (following Clayton's theory; Fig. 1a) or a cyclonic (following Aplin and Harrison's theory; Fig. 1b) influence on near-surface wind directions. We hypothesized that during maximum occultation (66–70% across Switzerland, ≈2000 km away from the umbral center), Switzerland was in the ideal position to determine which of the two theories is closer to reality. Our aim in this paper is thus to extend the analysis of temperature drops during occultation to assess whether available wind direction data can support one of the two theories about air mass circulation inside the penumbra during the eclipse.

2 Material and Methods

The vernal equinox eclipse of 20 March 2015 was a Saros 120 total eclipse (partial in Switzerland), with its maximum at 09:45:39 UTC (10:45:39 CET; NASA, 2015). In Switzerland, occultation started with the first contact of the sun and moon disks at 09:21:58 CET in Geneva (western border) and ended with the fourth contact at 11:47:49 CET in Martina (eastern border). Maximum occultation ranged from 65.8% in Chiasso (southern border) to 70.1% in Bargen/Schaffhausen (northern border). The timing of maximum occultation varied from 10:29:26 to 10:35:55 CET across Switzerland (NASA, 2017). The

second and third contact of a total eclipse are the entering into and exiting from the umbra, respectively. In areas with only partial occulation, the second and third contact do not occur.

This eclipse has been thoroughly investigated with a focus on the mainland UK in a themed issue with 16 papers introduced by Harrison and Hanna (2016). Although all contributions are relevant, we specifically refer only to the articles with a direct link to our own study (Aplin et al., 2016; Clark, 2016; Good, 2016; Hanna et al., 2016; Burt, 2016; Pasachoff et al., 2016; Gray and Harrison, 2016; Portas et al., 2016; Barnard et al., 2016).

2.1 Sites and data

We used six Swiss FluxNet sites (www.swissfluxnet.ch; Table S1) with 20 Hz ultrasonic anemometer–thermometer data and 184 conventional MeteoSwiss weather stations (Table S2) across Switzerland and Liechtenstein (MeteoSwiss, 2017), of which 165 not only provided temperature data but also wind speed and wind direction measurements (Table S3). We used data from 20 March 2015 and—where possible—the previous one or two days for reference. All three days were nearly clear, except for occasional scattered high-level clouds.

Sensors used at the MeteoSwiss station are Pt-100 thermistors for temperature measurements and Lamprecht L14512 cup anemometers with a wind vane for wind speed and wind direction measurements. Some sites alternatively use 2-D ultrasonic anemometers (MeteoSwiss, 2017). At the Swiss FluxNet sites, the specific instruments included in this study were Gill HS or R3 ultrasonic anemometers (Gill Ltd., Lymington, UK), Kipp and Zonen CNR-1 four-way net-radiometers (Delft, the Netherlands) with active ventilation (Markasub, Olten, Switzerland). Only at the CH-OE2 site, a Delta-T BF5 sunshine sensor (Cambridge, UK) was available for measurements of diffuse and total photosynthetic photon flux density (PPFD). PPFD is the quantum flux in the visible range 400–700 nm that plants use for photosynthesis.

For all these variables except temperature (see Section 2.2) and wind direction (see Section 3.4), the difference between 20 March and either 18 or 19 March was calculated, depending on which of the two previous days had closer to clear-sky conditions. We used two different concepts to determine the drop in temperature (see Section 2.2).

2.2 Calculation of temperature drop

All analyses were done with R version 3.3.1 (R Core Team, 2016). The local temperature effect at each site was estimated by fitting a local polynomial regression with a span parameter of 0.1 (“loess”, a locally weighted least squares regression function in R) to each time series from 20 March. The measurements during the penumbral shading and the adjacent 12 minutes on both sides were excluded from the fit. The maximum difference between the measurements during penumbral shading and these fitted values was then determined. This approach closely followed the method used by Segal et al. (1996), or the linear approach used by Clark (2016). In a few cases (sites GRH, ROG, ULR, VAD, VSBLI; see Table S2), however, this approach failed (e.g. because of instationarity shortly before, shortly after, or during the time period of the eclipse, which can lead to erratic interpolations) and thus the simple temperature difference with respect to 19 March was used. We did not use this latter approach for all sites because there were substantial temperature differences between 18, 19 and 20 March 2015, despite persistent and very similar fair-weather conditions. The period of interest coincided with the peak spring snowmelt. For

example, at the CH-FRU mountain grassland flux site (1000 m a.s.l.) where four phenological camera images were taken per day, the snow cover in the morning of 18 March 09:30 CET was still around 80%, but declined strongly during 18/19 March and had less than 10% coverage by the evening of 19 March at 18:30 CET. On 20 March, the site was basically free of snow, similar to other mountainous stations that were subject to snowmelt.

3 Results and Discussion

3.1 Short-wave radiation effects

Incoming short-wave radiation can be used as a control for correct timing and magnitude of the occultation. Standard MeteoSwiss weather stations, however, only record 10-minute averages, which are too coarse for an in-depth assessment. The Swiss FluxNet sites use averaging times ranging from 10 to 30 minutes (Table S1), with the exception of the CH-OE2 cropland and CH-DAV forest sites where 1-minute averages of all four radiation components were available. Diffuse and total PPFD were also measured with the same resolution at CH-OE2, and thus we used data from CH-OE2 as an example here. The expected reduction of incoming short-wave radiation was ≈70% (Fig. 2a) during maximum occultation of the sun's disk (≈70%). The difference between measured and expected incoming short-wave radiation was –9.8 ± 0.7 W m^{-2} (mean ± SE). For a second class pyranometer such as the CM3 model used in the CNR-1 radiometer, this is the order of magnitude of the accuracy. However, the timing of the radiation minimum in Figure 2a was not exactly as expected assuming that minimum radiation should be observed at the time of maximum occultation: the theoretical radiation level during maximum occultation was reached 19 minutes before the eclipse's maximum. Most likely, this was a confounding effect due to minor high-level Cirrostratus clouds passing at that time; the fraction of diffuse radiation already started to increase shortly after the first contact on 20 March (Fig. 2b), whereas on the previous day, a curvilinear decrease was observed as expected during this early morning period with rising solar elevation. Cirrostratus clouds are the likely cause since images taken every two minutes during the occultation phase at the site do not indicate any signs of medium and low-level clouds. This coincidence of shading by cirrostratus clouds and occultation of the sun may have led to the stronger than expected decrease in short-wave radiation levels and the earlier than expected radiation minimum.

To test this hypothesis, we made an attempt to empirically correct measured short-wave incoming radiation for potential concurrent cloud shading that leaves a trace in the fraction of diffuse radiation (Fig. 2c). The assumption we made for such a correction was that no change in the ratio of diffuse vs. direct radiation would occur due to the occultation of the sun's disk alone. Thus, if we assume that the diffuse radiation (expressed as absolute radiation flux density) remains unaffected by the cirrostratus clouds, then we can correct this effect with

$$SW_{in,\,corr} = \frac{\alpha}{\alpha_{fit}} \cdot SW_{in}\ , \tag{1}$$

where SW_{in} and $SW_{in,\,corr}$ are measured and corrected incoming short-wave radiation, and α and α_{fit} are ratios of diffuse and direct radiation for the measurements and the model, where the empirical best fit for α_{fit} used in the model (Fig. 2c) is

$$\alpha_{fit} = \frac{\textit{diffuse radiation}}{\textit{direct radiation}} = (0.674 \pm 0.002) + (0.0452 \pm 0.0002) \cdot (\Delta t)^2\ , \tag{2}$$

with Δt being the time difference to local noon (12:36:45 CET on 20 March 2015) in hours. This empirical fit was used because α was not a simple function of the solar elevation angle (fit not shown). The resulting $SW_{in,\,corr}$ (red line in Fig. 2a) still did not show a symmetric effect before and after the short-wave radiation minimum. An analysis of images during that period (Fig. 2d) also indicated that the shading effect was not symmetric during occultation: the image brightness decreased very quickly after first contact, but then remained almost constant, irrespective of the fraction of occultation of the sun's disk. This potential effect of cloudiness during the eclipse was investigated by analyzing the brightness of the vegetation in a sequence of phenological camera images that were recorded every two minutes during the eclipse (4× per day otherwise). For this, we used the ImageJ software as implemented in the Fiji image processing package, version 2.0.0 (http://imagej.net/Fiji). The vegetation brightness is simply the normalized gray value of the image region that was manually defined as "vegetation". A brightness of 100% corresponds to a white image, and 0% is black.

Both observations—diffuse/direct radiation measurements and camera images—indicated a confounding effect of cirrostratus cloud passage.

3.2 Long-wave radiation effects

To quantify the eclipse effect on long-wave back-radiation from the sky (sometimes referred to as "longwave albedo") we determined the difference between the two long-wave flux components from 20 March 2015 and the reference day before,

$$\Delta LW_x = LW_x(\text{20 March}) - LW_x(\text{19 March})\,, \tag{3}$$

where x is the incoming (in) or the outgoing (out) long-wave radiation component. Then, two linear regressions between ΔLW_{in} and ΔLW_{out} were calculated with the 1-minute averages of the CH-OE2 site, (a) for the period of the eclipse (09:26–11:42 CET), and (b) for the times of day not including the period of the eclipse.

The reduction in short-wave radiation also reduced energy dissipation at Earth's surface, which in turn reduced long-wave emitted radiation (LW_{out}, Fig. 2e, blue line). The reduction in LW_{out} was symmetric during the penumbral shadow passage, supporting our interpretation that if a cloud passage confounded the SW_{in} term, then it most likely was a cloud type that affected short-wave radiation more than the long-wave radiation components. Cirrostratus may have this quality. However, the role of high clouds on Earth's radiation budget is difficult to quantify (Boucher et al., 2013).

The reduction in LW_{out} reduced the re-emitted sky radiation LW_{in} (Fig. 2e, black line). The regression between ΔLW_{in} and ΔLW_{out} (Fig. 3), i.e., the differences between the respective radiation component measured on the day of the eclipse and the day before the eclipse, showed an order of magnitude difference between the penumbral shading ($\Delta LW_{in} \approx 0.24\ \Delta LW_{out}$) and the unshaded conditions ($\Delta LW_{in} \approx 2.84\ \Delta LW_{out}$).

3.3 Direct effects on air temperature

Although radiation effects could be investigated at only the two sites having 1-minute measurements, similar conditions were observed in 10-min data at all radiation measurement sites. All sites showed a reduction in 2-m air temperatures (Table S2). The strongest effect of –5.8 K was seen at an Alpine site (Fig. 4; VSSOR in Table S2) at 1987 m a.s.l. which was still

completely snow covered during the eclipse. The topographic setting (Fig. 4) is a small basin surrounded by a larger catchment area of 7.5 km^2. The most important effect thus appeared to be the position of the weather station. It was located in a closed topographical basin ca. 66 m below the mountain ridge. A cold-air pool building up during the eclipse could be drained towards the Rhone valley over this ridge. Had we taken the difference between 19 and 20 March for estimating the temperature effect, then this site would have yielded a difference of –8.8 K.

To quantify the uncertainty of the temperature drop (and wind direction effects) as a function of elevation, we employed nonparametric bootstrapping with the Bootstrap Resampling package of R in combination with the "loess" function with a span of 0.5 to describe the temperature drop or wind direction effect as a function of elevation. Elevations were binned in 10-m intervals for the bootstrap procedure, which was repeated 9,999 times. Statistical confidence intervals were then determined from the output at the 95% level. Bootstrapping is an efficient computer-based method to quantify uncertainty intervals (e.g. Efron, 1979; Johns, 1988). Nonparametric bootstrapping means that the uncertainty calculations are done on randomly selected subsets of all data points available in such a way that the variation in the results obtained from many repetitions (9,999 repetitions in our case) represents the uncertainty of the estimate.

The mean effect over the entire elevation range covered by MeteoSwiss weather stations (Table S2) as determined by non-parametric bootstrapping was a reduction of 1.51 ± 0.02 K (mean $\pm$ SE; see Fig. 5). The weakest effects were found at the lowest elevation sites (<350 m a.s.l., reduction of 0.62 ± 0.06 K), and the highest elevation sites, where data coverage was poor (>3150 m a.s.l., reduction of 0.69 ± 0.03 K).

Although the 20 March 2015 eclipse featured a partial occultation of 66–70% throughout Switzerland, the temperature effects (Fig. 5, Table S2) were comparable to temperature reductions previously reported in the literature for all eclipse types (Fig. 6 and Table 1). We found no clear dependence of temperature reductions on eclipse type, geographic location or other factors in the literature reports. Therefore, we summarized the data set by fitting a Gamma probability distribution to the data as shown in Figure 6. The Gamma probability density function

$$f(\Delta T) = \frac{1}{s^a \cdot \Gamma(a)} \cdot (\Delta T - T_0)^{a-1} \cdot e^{\frac{T_0 - \Delta T}{s}} \tag{4}$$

was fit to the histogram of the maximum cooling ΔT during the eclipse, where ΔT is the maximum temperature drop during an eclipse event (a positive value), and a and s are the shape and scale parameters of the probability density function $f(\Delta T)$, respectively. Γ is the Gamma function, and T_0 is the reference value (or offset) of ΔT to fit the peak of the probability density function $f(\Delta T)$ to the data. The distribution developed in this study will allow researchers to quickly assess the probability that the existing literature contains values that exceed a given measured temperature drop during an eclipse. The parameter estimates for the probability distribution (Eq. 4) are given in Table 2. The average temperature drop reported in the literature thus far was 2.6 ± 1.7 K (based on Eq. 4, Table 2), while the mean drop calculated for our study was 1.5 ± 1.0 K. Already temperature effects of this (smaller) magnitude during occultation have the potential to induce thermal winds.

3.4 Wind direction effects

The effect of penumbral shading on wind direction was determined by comparing (a) the 1-hour reference period that ended 12 minutes before the first contact with (b) the first half of penumbral shading (from first contact to maximum occultation, which was roughly 1.1 hour). For both periods, the vector-averaged mean wind direction was computed, and then the rotation angle was determined. The same procedure was repeated for the same time periods of 19 March, and the difference in rotation angle was calculated as the net effect of penumbral shading used in this study.

The most striking effect on wind direction was found at two Swiss FluxNet sites with high-resolution 3-D wind velocity measurements. The timing of the solar eclipse between 09:22 and 11:48 CET across Switzerland (see Section 2) coincided with the hours when the mountain valley wind system typically changes direction by 180° under normal conditions. A mountain valley wind system is characterized by down-valley winds at night that contrast with up-valley winds during the day when solar irradiation on the mountain slopes leads to convective uplifting of air masses, thereby leading to up-slope and up-valley winds. At night, the radiative cooling on the same valley slopes leads to the production of cold air, which is denser than the surrounding air, and hence moves down-slope and down-valley (also known as katabatic drainage flow). At the CH-DAV subalpine forest site (1639 m a.s.l.), the penumbral shading resulted in a delay of the onset of the daytime wind direction by roughly one hour (Fig. 7), whereas at the CH-AWS alpine grassland site (1978 m a.s.l.) the shading even prevented the establishment of the diurnal up-valley wind altogether (Fig. 7). From 09:26:32 CET (first contact) to 11:46:37 CET (last contact), the short-wave radiation decreased by up to 68% (–447 $\mathrm{W\,m^{-2}}$; 10-minute average) with respect to perfect clear-sky conditions two days before (18 March 2015). This delayed the down-valley to up-valley wind direction transition that had been pronounced on both preceding days. Further, the penumbral shading hindered the onset of up-valley winds in such a way that the down-valley winds persisted even after the shading had ended. This means that the valley wind blew in the opposite direction to what we would have predicted for comparable conditions without penumbral shading. The lack of reversal of wind direction could have been an effect of the cyclonic rotation in the outer circle of the penumbra as predicted by Aplin and Harrison (2003) for this distance of ≈2000 km from the umbra. This lack of reversal of wind direction at CH-AWS also occurred at a conventional agrometeorological weather station ca. 1 km further up-valley Michna et al. (2013).

Although the cyclonic effect appeared to be rather pronounced at CH-DAV and even more so at CH-AWS, most conventional weather stations did not show a clear signal (Figs S1–S4). In principle, only sites located on a valley bottom (Fig. S2) are expected to respond in a similar way as CH-DAV and CH-AWS. In fair weather conditions winds at slope sites (Fig. S4) typically rotate clockwise when on the right sidewall of a valley (i.e, facing down-valley) and counterclockwise on the left sidewall, as winds undergo their diurnal transitions from along-valley to along-slope wind systems (Whiteman, 2000). Thus, the inclusion of slope sites in our analysis would confound our analysis of the wind turning associated with the eclipse passage. The sites classified as “slope sites” (Table S3) turned out to be embedded in rather complex terrain for which it was impossible to make a reasonable prediction which rotation should be expected. Consequently, we focus primarily on the sites not located on slopes in the following analysis.

The wind direction effect during the eclipse observed at the 165 MeteoSwiss sites included both anticyclonic and cyclonic changes (Fig. 8, green bars). If slope sites were excluded from the analysis, then a rather clear dominance of the cyclonic effect was seen (68.7% of the remaining 112 sites; Fig. 8, black bars). In comparison to conditions during the same time of day on the day before the eclipse, the directional changes were mostly in the range –30° to –45° during the period from the first contact to maximum occultation (Fig. 8). Large direction changes exceeding –75° were less frequent than on the reference day before the eclipse.

The effect of the penumbral shading on wind direction at 10 m a.g.l. showed a strong dependence on site elevation. Figure 9 showed an elevational integration of the percentage of sites showing cyclonic influence during the penumbral shading as expected according to Aplin and Harrison (2003) (Fig. 1b). There was only one elevation zone (1708–2730 m a.s.l., 14 sites) in which a significant cyclonic rather than anticyclonic influence ($p<0.05$ according to bootstrapped uncertainty bounds) was found. The eclipse effect seen at the sites in this elevation zone was clearly in support of the revised theory by Aplin and Harrison (2003), which reduced the extent of the anticyclonic outflow around the umbra from ≈2400 km Clayton (1901) to ≈1600 km (Fig. 1). Interestingly, however, Hanna et al. (2016) did not find any discernible effect of this eclipse on wind directions in the UK and Iceland, and thus deduced that there was no evidence of an eclipse cyclone. In contrast to Switzerland, the UK observed a fair share of cloudiness (see satellite imagery in Hanna et al., 2016) which may have muted some meteorological responses to the occultation, as Burt (2016) noted. But when the analysis was constrained to sites with clear-sky conditions, Gray and Harrison (2016) found a clear cyclonic effect of approximately 20–40° in the comparison of surface measurements with forecast model simulations which were ignorant of the eclipse. While such a cyclonic effect is what would be expected for Switzerland following the theory of Aplin and Harrison (2003), it contradicts this theory for the geographic location of the British Islands. Here, anticyclonic modification of the wind direction should have been observed under both Clayton (1901) and Aplin and Harrison (2003) theories. Hence, Gray and Harrison (2016) offer a new interpretation similar to the nocturnal low level jet. This interpretation is however not likely to explain conditions in the complex terrain for the Swiss Alps because low level jets develop primarily on the Swiss Plateau (Ihly, 1995), not in the Alpine valleys. Hence we did not further adopt this interpretation here.

3.5 Spatial patterns of wind direction effects

Wind direction effects were spatially interpolated with ordinary Kriging using the krige.conv function of the geoR package of R. The partial sill parameter was set to 300°, and the range parameter was set to 1000 km. We tested the range 90°–300° for the partial sill setting, and 10–10,000 km for the range setting. The results were similar due to the optimization method used in Kriging and differed only in very minor details (see examples in our response, doi:10.5194/acp-2017-321-AC2). The selection for the final computations was thus based only on the facts that a 300° (or –60°) corresponded to the typical deviation angle of wind directions under cyclonic influence, and that 1000 km covered the entire domain of Switzerland.

To test if there existed a geographically consistent pattern of wind direction changes across Switzerland and Liechtenstein we performed a spatial interpolation (Fig. 10). For the reasons given above, we again focused on sites that were not located on slopes (Fig. 10b). The resulting map, however, is relatively similar to the one using all sites (Fig. 10a).

If all stations were considered irrespective of their individual topographic environment (Fig. 10a), then a complex pattern emerged that did not show a clear spatial structure that could be related to the passing of the penumbral shadow. Also valley bottom sites (Fig. 10e) showed a mixture of anticyclonic effects in the west, south of the Alps, and eastern Switzerland, with cyclonic effects seen between these three anticyclonic areas. Sites on flat ground without clear topographic influences (Fig. 10c) showed cyclonic effects in the center of Switzerland, surrounded by anticyclonic effects namely in the Valais (southwestern Switzerland) and the northeast. Mountain top and hilltop sites (Fig. 10d) showed yet another pattern, with anticyclonic influences seen mostly in the western half of Switzerland and cyclonic effects in the eastern half. The only group of sites showing a consistent spatial pattern were those in the elevation range 1708–2730 m a.s.l. (Fig. 10f), the ranges with a statistically significant preference for cyclonic effects in Figure 9. This cyclonic effect was seen across most of Switzerland, with the exception of a few high mountain sites in the Grisons (eastern Switzerland), the part of the study domain that was farthest away from the trajectory of the eclipse (Fig. 1). This high elevation range corresponded to the level where the influence of the topographical roughness of the Swiss mountains vanished in vertical radiosonde profiles (at ≈2500 m, Wanner and Furger, 1990).

Taken together, these findings support the hypothesis that Switzerland was in the cyclonic part of the penumbral shading as expected from the Aplin and Harrison (2003) theory (Fig. 1b), and not within the anticyclonic part as would be expected from the Clayton (1901) theory (Fig. 1a). Although no theory exists on how the transition zone between the inner anticyclonic and the outer cyclonic ring around the umbra should affect local wind directions, our analysis indicated that the effect was most likely a combination of distance from the center combined with the meso- and micro-scale topography around the site. This is not unexpected if the net effect of the shading is weak. The fact that there was a significant preference for cyclonic effects at sites in the elevation range 1708–2730 m a.s.l., whereas there was no significant difference between anticyclonic and cyclonic effects at other elevations, suggested that the reduced dimensions of the anticyclonic band around the umbra as proposed by Aplin and Harrison (2003) is more likely to be correct than the original Clayton (1901) model, in which Switzerland should have experienced a shift from cyclonic to anticyclonic influence as the occultation progressed towards its local maximum.

3.6 Comparison with findings from other eclipses

The present study expands previously published analyses of the eclipse effect using multiple stations in a given region. For example Brazel et al. (1993) performed a similar analysis of temperature effects using 16 weather stations in the Phoenix, Arizona, metropolitan area, but were unable to analyse wind direction effects. They mentioned two reasons why this was not feasible: (1) the eclipse occured in the morning when the wind flow tends to reverse due to topographic heating in the Salt River Valley, and (2) several of the available stations did not record wind direction, but only wind speed. The first point (given with reference to Frenzel, 1963) is typical for any topographically varying region on the globe and exactly matches the conditions experienced in this study. This effect was also emphasized by Anderson (1999), Vogel et al. (2001), and Sjöblom (2010): surface cooling can trigger downslope and katabatic winds in mountainous regions, such as the Alps, the Arctic islands and Antarctica.

On 18 to 20 March 2015, synoptic pressure conditions over the European Alps showed a persistent high-pressure band between the UK and Russia, providing an excellent basis for comparing conditions during the solar eclipse with previous days.

Although such comparisons are one of the most used approaches to quantify the effects of solar eclipses (Owen and Jones, 1927; Shur, 1984; Brazel et al., 1993; Jain et al., 1997; Dutta et al., 1999; Dolas et al., 2002; Gorchakov et al., 2007; Chernogor, 2008; Gorchakov et al., 2008; Sjöblom, 2010; Bala Subrahamanyam and Anurose, 2011; Bala Subrahamanyam et al., 2011; Muraleedharan et al., 2011; Bala Subrahamanyam et al., 2012; Murthy et al., 2013), in most cases weather conditions are rather variable and nonideal for direct comparisons. In Switzerland, the 20 March 2015 eclipse occurred when snow cover was disappearing at mountain locations around 1000 m a.s.l., and thus air temperatures varied more strongly from day to day than what would be desirable for estimating temperature effects. Therefore, we employed the less widely used approach by Segal et al. (1996) to fit a curvilinear interpolation over the period of occultation from first to fourth contact. This approach is typical for assessing effects on atmospheric constituents such as ozone (Tzanis et al., 2008). A third approach to deal with the variability of measurements during reference days is to take the 30-day hourly median values for comparison (Gerasopoulos et al., 2008). All three approaches have advantages and disadvantages. In our case, the direct comparison with the day before the eclipse during which similar synoptic weather conditions persisted would have led to a more pronounced temperature drop by an additional 1.3 K on average. The relationship between the temperature drop of all sites reported in Table S2 as used in our study and the absolute difference to the day before the eclipse was

$$\Delta T_{19} = -2.06 \pm 0.17 + (0.48 \pm 0.09)\Delta T\,, \tag{5}$$

with ΔT being the temperature drop used in this study and ΔT_{19} being the alternative calculation of ΔT as the difference between the measurements made on 20 March and the same time of day on 19 March (the day before the eclipse; $p < 0.001$, adj. $R^2 = 0.124$).

The choice of method to determine the temperature drop—and any other variable of interest affected by the penumbral shading—has a substantial effect on the result, not only in our study, but also in other published results (e.g. Table 1). Only 9% of the published studies reported stronger temperature effects than the most extreme 5.8 K drop at the Sorniot–Lac Inférier site reported here, although most temperature drop reports in the literature relate to maximum occultation during total and annular eclipses. During future eclipses it may now become possible to engage citizen scientists to determine the temperature drop during an eclipse and relate it to the probability distribution presented in Table 3 or to the Gamma distribution of Eq. (4) and Table 2, which would put their measurements into context (see also Portas et al., 2016; Barnard et al., 2016).

Differences in temperature drops among different eclipse events depend on the solar elevation at the time of the eclipse (Reynolds, 1937). Here we showed that although the eclipse happened in the morning hours and although occultation was only partial across Switzerland, substantial drops in air temperatures at several Swiss sites (Table S2) exceeded those observed at other locations with higher solar angles (Table 1). Thus, our results suggest that the topographic setting, not the geographic position on the globe, may actually be the most important determinant of the temperature drop for individual sites.

With respect to wind direction effects, few studies are available for comparison, with Clayton (1901) still being a classical reference after more than one century. Regional weather forecast models are now run at a spatial resolution that should theoretically allow simulations of the effect of penumbral shading on wind speed (not assessed here due to inconsistent variability among the sites) and wind direction (as presented in Fig. 10). Gray and Harrison (2012) followed this approach for the southern

UK during the 11 August 1999 eclipse, but found that the umbral shading did not produce clear effects on wind vectors. They concluded that the primary response of the model was restricted to temperature. Similarly, Prenosil's (2000) simulations for Central Europe showed model responses for temperature and humidity, but not for near-surface winds. Few wind observations are available for testing of such models, and Prenosil (2000) concluded that special observation campaigns with very accurate sensors would be required to make progress. The six Swiss FluxNet sites provided detailed measurements, and many more sites are available globally via Fluxnet (Baldocchi et al., 2001). However, the Fluxnet sites provide only aggregated 30-minute averages, not the raw data at original resolution. Of our six sites with available high-frequency measurements, two sites (CH-DAV and CH-AWS, Fig. 7) showed a clear wind direction effect during the penumbral shading, even though the distance to the center of the eclipse was on the order of 2000 km.

4 Conclusions

Temperature responses to the eclipse were quite strong (up to 5.8 K cooling, 1.51 ± 0.02 K on average), especially in basin topography where the cold air from the occultation can pool. Our results suggest that the topographic setting was the most important determinant of the temperature drop for individual sites. Effects on wind directions were variable and site-specific as well. Thermo-topographic winds generated in the penumbral zone of a solar eclipse can modify local wind systems, either by delaying of the onset of the diurnal wind shift (as seen at the CH-DAV site) or by preventing the establishment of an up-valley wind in mountainous areas (at the CH-AWS site). These effects can occur at a considerable distance from the umbral path and two theories exist on the wind direction effect at a distance of $\approx$2000 km from the center of the eclipse (Fig. 1). According to Clayton (1901), an anticyclonic outflow should extend up to 2400 km from the center of the eclipse, which would include all of Switzerland during the 20 March 2015 eclipse. The modified theory by Aplin and Harrison (2003) reduces this extent to 1600 km, which would exclude all of Switzerland during the 20 March 2015 eclipse and leave it in the outermost ring with cyclonic counterflow. Our analyses more strongly supported the latter theory, at least for the elevation range 1706–2750 m a.s.l. (the elevations at which the typical influence of the roughness of the mountain topography tended to vanish). In this elevation zone, the influence of the penumbral shading on near-surface wind directions was detectable even at distances greater than 2000 km from the center of the umbra, at places where maximum occultation during an eclipse was as low as 66–70%.

5 Data availability

Our data policy is available under http://www.gl.ethz.ch/research/data-archive.html. Aggregated Swiss FluxNet data are directly available from the European Flux Database Cluster (http://gaia.agraria.unitus.it/pi-area; 30-min averages). Binary raw data files, ancillary data at finer resolution than 30-min, and phenological camera images are available from the corresponding author on request. The MeteoSwiss data are directly available via their IDAWEB interface (https://gate.meteoswiss.ch/idaweb?language=en; registration required; freely available for non-commercial research projects).

Author contributions. WE designed the study, carried out all analyses, wrote and revised the manuscript. CDW provided essential topo-climatological input and advice for the analyses. All co-authors were involved in writing and contributed to the article with feedback and critique.

Competing interests. None.

Acknowledgements. This study made extensive use of standard meteorological data collected by MeteoSwiss, the Swiss Federal Office for Meteorology and Climatology, which also contains sites from the Swiss Airforce (Kdo LVb FULW 34) and the Swiss Federal Research Institute WSL. We acknowledge the use of these data via the IDAWEB online database. We thank Jon Eugster, University of Zurich, for mathematical support with probability distribution model implementation. The Swiss National Science Foundation (SNF) supported research at the CH-OE2 Swiss FluxNet site via grant 146373, at the CH-DAV site via grant 148992 (ICOS-CH), and at the CH-CHA and CH-FRU sites via grant 154245.

References

Anderson, J.: Meteorological changes during a solar eclipse, Weather, 54, 207–215, 1999.

Anderson, R. C. and Keefer, D. R.: Observation of the temperature and pressure changes during the 30 June 1973 solar eclipse, J. Atmos. Sci., 32, 228–231, 1975.

Anderson, R. C., Keefer, D. R., and Myers, O. E.: Atmospheric pressure and temperature changes during the 7 March 1970 solar eclipse, J. Atmos. Sci., 29, 583–587, 1972.

Anonymous: Meteorological Observations during the Solar Eclipse of 30th November, Boston Medical and Surgical Journal, 11, 295–296, 1834.

Aplin, K. and Harrison, R.: Meteorological effects of the eclipse of 11 August 1999 in cloudy and clear conditions, Proc. R. Soc. Lond. A, 459, 353–371, doi:10.1098/rspa.2002.1042, 2003.

Aplin, K. L., Scott, C. J., and Gray, S. L.: Atmospheric changes from solar eclipses, Phil. Trans. R. Soc. A, 374, 20150 217, doi:10.1098/rsta.2015.0217, 2016.

Ashworth, J.: Fall of temperature during the solar eclipse, Nature, 120, 227, 1927.

Bala Subrahamanyam, D. and Anurose, T.: Solar eclipse induced impacts on sea/land breeze circulation over Thumba: A case study, J. Atmos. Sol. Terr. Phys., 73, 703–708, doi:10.1016/j.jastp.2011.01.002, 2011.

Bala Subrahamanyam, D., Anurose, T., Mohan, M., Santosh, M., Kiran Kumar, N. V. P., Sijikumar, S., Prijith, S. S., and Aloysius, M.: Atmospheric surface-layer response to the annular solar eclipse of 15 January 2010 over Thiruvananthapuram, India, Bound.-Layer Meteorol., 141, 325–332, doi:10.1007/s10546-011-9627-z, 2011.

Bala Subrahamanyam, D., Anurose, T., Mohan, M., Santosh, M., Kiran Kumar, N., and Sijikumar, S.: Impact of annular solar eclipse of 15 January 2010 on the atmospheric boundary layer characteristics over Thumba: A case study, Pure Appl. Geophys., 169, 741–753, doi:10.1007/s00024-011-0336-9, 2012.

Baldocchi, D., Falge, E., Gu, L., Olson, R., Hollinger, D., Running, S., Anthoni, P., Bernhofer, C., Davis, K., Evans, R., Fuentes, J., Goldstein, A., Katul, G., Law, B., Lee, X., Malhi, Y., Meyers, T., Munger, W., Oechel, W., Paw U, K. T., Pilegaard, K., Schmid, H. P., Valentini, R., Verma, S., Vesala, T., Wilson, K., and Wofsy, S.: FLUXNET: A new tool to study the temporal and spatial variability of ecosystem-scale carbon dioxide, water vapor, and energy flux densities, Bull. Am. Meteorol. Soc., 82, 2415–2434, 2001.

Barnard, L., Portas, A. M., Gray, S. L., and Harrison, R. G.: The National Eclipse Weather Experiment: an assessment of citizen scientist weather observations, Phil. Trans. R. Soc. A, 374, 20150 220, doi:10.1098/rsta.2015.0220, 2016.

Bilham, E. G.: Meteorological observations during the annular solar eclipse of April 8th 1921, Q. J. R. Meteorol. Soc., 47, 206–210, doi:10.1002/qj.49704719907, 1921.

Boucher, O., Randall, D., Artaxo, P., Bretherton, C., Feingold, G., Forster, P., Kerminen, V.-M., Kondo, Y., Liao, H., Lohmann, U., Rasch, P., Satheesh, S. K., Sherwood, S., Stevens, B., and Zhang, X. Y.: Clouds and Aerosols, In: Stocker T. F., Qin D., Plattner G.-K., Tignor M., Allen S. K., Boschung J., Nauels A., Xia Y., Bex V. and Midgley P. M. (eds.), Climate Change 2013: The Physical Science Basis. Contribution of Working Group I to the Fifth Assessment Report of the Intergovernmental Panel on Climate Change, Cambridge University Press, Cambridge, United Kingdom and New York, NY, USA, 2013.

Brazel, A., Cerveny, R., and Trapido, B.: Localized climatic responses during the 11 July 1991 eclipse: Phoenix AZ, Climatic Change, 23, 155–168, doi:10.1007/BF01097335, 1993.

Burt, S.: Meteorological responses in the atmospheric boundary layer over southern England to the deep partial eclipse of 20 March 2015, Phil. Trans. R. Soc. A, 374, 20150214, doi:10.1098/rsta.2015.0214, 2016.

Chernogor, L.: Effects of solar eclipses in the surface atmosphere, Izvestiya – Atmos. Ocean Phys., 44, 432–447, doi:10.1134/S000143380804004X, 2008.

Clark, M. R.: On the variability of near-surface screen temperature anomalies in the 20 March 2015 solar eclipse, Phil. Trans. R. Soc. A, 374, 20150213, doi:10.1098/rsta.2015.0213, 2016.

Clayton, H. H.: The eclipse cyclone and the diurnal cyclones, Annals of the Astronomical Observatory of Harvard College, 18, 1–31, 1901.

Dolas, P. M., Ramchandran, R., Gupta, K. S., Patil, S. M., and Jadhav, P. N.: Atmospheric surface-layer processes during the total solar eclipse of 11 August 1999, Bound.-Layer Meteorol., 104, 445–461, 2002.

Dutta, G., Joshi, M., Pandarinath, N., Bapiraju, B., Srinivasan, S., Subba Rao, J., and Aleem Basha, H.: Wind and temperature over Hyderabad during the solar eclipse of 24 Oct. 1995, Indian J. Radio Space Phys., 28, 11–14, 1999.

Economou, G., Christou, E., Giannakourou, A., Gerasopoulos, E., Georgopoulos, D., Kotoulas, V., Lyra, D., Tsakalis, N., Tzortziou, M., Vahamidis, P., Papathanassiou, E., and Karamanos, A.: Eclipse effects on field crops and marine zooplankton: The 29 March 2006 total solar eclipse, Atmos. Chem. Phys., 8, 4665–4676, 2008.

Efron, B.: Bootstrap methods: another look at the jackknife, The Annals of Statistics, 7, 1–26, 1979.

Fernández, W., Castro, V., and Hidalgo, H.: Air temperature and wind changes in Costa Rica during the total solar eclipse of July 11, 1991, Earth, Moon, and Planets, 63, 133–147, doi:10.1007/BF00575102, 1993a.

Fernández, W., Castro, V., Wright, J., Hidalgo, H., and Sáenz, A.: Changes in solar irradiance and atmospheric turbidity in Costa Rica during the total solar eclipse of July 11, 1991, Earth, Moon, and Planets, 63, 119–132, doi:10.1007/BF00575101, 1993b.

Fernández, W., Hidalgo, H., Coronel, G., and Morales, E.: Changes in meteorological variables in Coronel Oviedo, Paraguay, during the total solar eclipse of 3 November 1994, Earth, Moon and Planets, 74, 49–59, 1996.

Ferrel, W.: A Popular Treatise on the Winds, John Wiley, New York, 2 edn., https://archive.org/details/cu31924003877606, 1890.

Founda, D., Melas, D., Lykoudis, S., Lisaridis, I., Gerasopoulos, E., Kouvarakis, G., Petrakis, M., and Zerefos, C.: The effect of the total solar eclipse of 29 March 2006 on meteorological variables in Greece, Atmos. Chem. Phys., 7, 5543–5553, 2007.

Frenzel, C. W.: The wind regime at Tucson and Phoenix and their relation to air pollution, J. AZ-NV Acad. Sci., 2, 98–103, 1963.

Gerasopoulos, E., Zerefos, C., Tsagouri, I., Founda, D., Amiridis, V., Bais, A., Belehaki, A., Christou, N., Economou, G., Kanakidou, M., Karamanos, A., Petrakis, M., and Zanis, P.: The total solar eclipse of March 2006: Overview, Atmos. Chem. Phys., 8, 5205–5220, 2008.

Good, E.: Satellite observations of surface temperature during the March 2015 total solar eclipse, Phil. Trans. R. Soc. A, 374, 20150219, doi:10.1098/rsta.2015.0219, 2016.

Gorchakov, G., Kadygrov, E., Isakov, A., Karpov, A., and Miller, E.: Influence of a solar eclipse on thermal stratification and the turbulence regime, Dokl. Earth Sci., 417, 1243–1246, doi:10.1134/S1028334X07080259, 2007.

Gorchakov, G., Kadygrov, E., Kortunova, Z., Isakov, A., Karpov, A., Kopeikin, V., and Miller, E.: Eclipse effects in the atmospheric boundary layer, Izvestiya – Atmos. Ocean Phys., 44, 100–106, doi:10.1007/s11485-008-1011-z, 2008.

Gray, S. and Harrison, R.: Diagnosing eclipse-induced wind changes, Proc. R. Soc. Lond. A, 468, 1839–1850, doi:10.1098/rspa.2012.0007, 2012.

Gray, S. L. and Harrison, R. G.: Eclipse-induced wind changes over the British Isles on the 20 March 2015, Phil. Trans. R. Soc. A, 374, 20150224, doi:10.1098/rsta.2015.0224, 2016.

Gross, P. and Hense, A.: Effects of a total solar eclipse on the mesoscale atmospheric circulation over Europe – A model experiment, Meteorol. Atmos. Phys., 71, 229–242, 1999.

Hanna, E., Penman, J., Jónsson, T., Bigg, G. R., Björnsson, H., Sjúrðarson, S., Hansen, M. A., Cappelen, J., and Bryant, R. G.: Meteorological effects of the solar eclipse of 20 March 2015: analysis of UK Met Office automatic weather station data and comparison with automatic weather station data from the Faroes and Iceland, Phil. Trans. R. Soc. A, 374, 20150 212, doi:10.1098/rsta.2015.0212, 2016.

Harrison, R. G. and Hanna, E.: Introduction: The solar eclipse: a natural meteorological experiment, Phil. Trans. R. Soc. A, 374, 20150 225, doi:10.1098/rsta.2015.0225, 2016.

Hayes, R.: Fall in air temperature during the solar eclipse of December 13–14, 1936, Nature, 139, 967–968, 1937.

Hurni, L., ed.: Atlas of Switzerland, Version 3, Swisstopo, Wabern–Bern, CD-ROM edn., www.atlasofswitzerland.ch, 2010.

Ihly, B.: Der grossräumige nordöstliche Jet in der unteren Troposphäre im Schweizer Mittelland, Lenticularis Verlag, Opfikon, Switzerland, 108 pp., 1995.

Jain, S., Arya, B., Singh, S., Tripathi, O., and Hamid, A.: Measurement of various atmospheric parameters during a total solar eclipse, Terrestrial, Atmospheric and Oceanic Sciences, 8, 371–384, 1997.

Johns, M. V.: Importance sampling for bootstrap confidence intervals, Journal of the American Statistical Association, 83, 709–714, 1988.

Leeds-Harrison, P., Youngs, E., and Blackburn, D.: Soil temperatures during the solar eclipse on 11 August 1999, Eur. J. Soil Sci., 51, 183–184, doi:10.1046/j.1365-2389.2000.00293.x, 2000.

Mauder, M., Desjardins, R., Oncley, S., and MacPherson, I.: Atmospheric response to a partial solar eclipse over a cotton field in Central California, J. Appl. Meteorol. Climatol., 46, 1792–1803, doi:10.1175/2007JAMC1495.1, 2007.

Menke, D. H.: Total eclipse over Karimata: An astronomical and meteorological event, Weatherwise, 41, 272–275, doi:10.1080/00431672.1988.9925277, 1988.

MeteoSwiss: Klimabulletin März 2015 (climate bulletin, in German only), http://www.meteoschweiz.admin.ch/content/dam/meteoswiss/de/Klima/Gegenwart/Klima-Berichte/doc/klimabulletin_maerz_2015.pdf, accessed 2017-10-06, 2015.

MeteoSwiss: SwissMetNet, the automatic monitoring network of MeteoSwiss, http://www.meteoswiss.admin.ch/home/measurement-and-forecasting-systems/land-based-stations/automatisches-messnetz.html, accessed 2017-01-05, 2017.

Michna, P., Eugster, W., Hiller, R., Zeeman, M. J., and Wanner, H.: Topoclimatological case-study of Alpine pastures near the Albula Pass in the eastern Swiss Alps, Geogr. Helv., 68, 249–263, doi:10.5194/gh-68-249-2013, 2013.

Mill, H. R.: Air temperature during the solar eclipse, Nature, 54, 391, 1896.

Muraleedharan, P., Nisha, P., and Mohankumar, K.: Effect of January 15, 2010 annular solar eclipse on meteorological parameters over Goa, India, J. Atmos. Sol. Terr. Phys., 73, 1988–1998, doi:10.1016/j.jastp.2011.06.003, 2011.

Murthy, B., Latha, R., Sreeja, P., and Dharmaraj, T.: Transient land breeze: Eclipse induced wind flow modifications-Observations over plant canopy, J. Atmos. Sol. Terr. Phys., 89, 33–39, doi:10.1016/j.jastp.2012.07.010, 2013.

NASA: https://eclipse.gsfc.nasa.gov/SEplot/SEplot2001/SE2015Mar20T.GIF, accessed: 2017-01-05, 2015.

NASA: Javascript Solar Eclipse Explorer, https://eclipse.gsfc.nasa.gov/JSEX/JSEX-EU.html, accessed: 2017-01-05, 2017.

Nufer, R. and Gfeller, P.: Messung der Lufttemperature während der totalen Sonnenfinsternis am 26. Februar 1998 bei Sinamaica (Venezuela), Orion, 286, 28, 1998.

Nymphas, E., Adeniyi, M., Ayoola, M., and Oladiran, E.: Micrometeorological measurements in Nigeria during the total solar eclipse of 29 March, 2006, J. Atmos. Sol. Terr. Phys., 71, 1245–1253, doi:10.1016/j.jastp.2009.04.014, 2009.

Owen, E. A. and Jones, H. I.: Potentials during the solar eclipse, Nature, 120, 120, doi:10.1038/120120a0, 1927.

Pasachoff, J. M., Peñaloza-Murillo, M. A., Carter, A. L., and Roman, M. T.: Terrestrial atmospheric responses on Svalbard to the 20 March 2015 Arctic total solar eclipse under extreme conditions, Phil. Trans. R. Soc. A, 374, 20160 188, doi:10.1098/rsta.2016.0188, 2016.

Penaloza-Murillo, M. and Pasachoff, J.: Air-cooling mathematical analysis as inferred from the air-temperature observation during the 1st total occultation of the Sun of the 21st century at Lusaka, Zambia, J. Atmos. Sol. Terr. Phys., 125–126, 59–77, doi:10.1016/j.jastp.2015.02.002, 2015.

Pleijel, H.: Observations of temperature and air humidity during the total solar eclipse 29 March 2006 at Side, Turkey, Meteorol. Z., 18, 107–109, doi:10.1127/0941-2948/2008/0324, 2009.

Portas, A. M., Barnard, L., Scott, C., and Harrison, R. G.: The National Eclipse Weather Experiment: use and evaluation of a citizen science tool for schools outreach, Phil. Trans. R. Soc. A, 374, 20150 223, doi:10.1098/rsta.2015.0223, 2016.

Prenosil, T.: The influence of the 11 August 1999 total solar eclipse on the weather over central Europe, Meteorol. Z., 9, 351–359, 2000.

R Core Team: R: A Language and Environment for Statistical Computing, R Foundation for Statistical Computing, Vienna, Austria, https://www.R-project.org/, 2016.

Reynolds, J. H.: Proceedings of the Meeting of the Royal Astronomical Society, The Observatory, 60, 1–8, 1937.

Segal, M., Turner, R., Prusa, J., Bitzer, R., and Finley, S.: Solar eclipse effect on shelter air temperature, Bull. Amer. Meteor. Soc., 77, 89–99, 1996.

Shur, G.: Aircraft investigation of the effect of a total solar eclipse on temperature, wind, and turbulence in the atmosphere, Soviet Meteorol. Hydrol., 6, 31–34, 1984.

Sjöblom, A.: A solar eclipse seen from the High Arctic during the period of midnight sun: Effects on the local meteorology, Meteorol. Atmos. Phys., 107, 123–136, doi:10.1007/s00703-010-0070-3, 2010.

Stoev, A., Stoeva, P., Kiskinova, N., and Stoyanov, N.: Evolution of the basic micrometeorological parameters during the total solar eclipse of 29 March 2006 at Manavgat, Turkey, Proc. of SPIE, 6936, doi:10.1117/12.783768, 2008.

Szalowski, K.: The effect of the solar eclipse on the air temperature near the ground, J. Atmos. Sol. Terr. Phys., 64, 1589–1600, doi:10.1016/S1364-6826(02)00134-7, 2002.

Tzanis, C., Varotsos, C., and Viras, L.: Impacts of the solar eclipse of 29 March 2006 on the surface ozone concentration, the solar ultraviolet radiation and the meteorological parameters at Athens, Greece, Atmos. Chem. Phys., 8, 425–430, doi:10.5194/acp-8-425-2008, 2008.

Venkat Ratnam, M., Shravan Kumar, M., Basha, G., Anandan, V., and Jayaraman, A.: Effect of the annular solar eclipse of 15 January 2010 on the lower atmospheric boundary layer over a tropical rural station, J. Atmos. Sol. Terr. Phys., 72, 1393–1400, doi:10.1016/j.jastp.2010.10.009, 2010.

Vogel, B., Baldauf, M., and Fiedler, F.: The influence of a solar eclipse on temperature and wind in the Upper-Rhine Valley – A numerical case study, Meteorologische Zeitschrift, 10, 207–214, doi:10.1127/0941-2948/2001/0010-0207, 2001.

Wanner, H. and Furger, M.: The Bise – Climatology of a regional wind north of the Alps, Meteorol. Atmos. Phys., 43, 105–115, doi:10.1007/BF01028113, 1990.

Ward, R. D.: Changes of temperature during the recent solar eclipse, Science, 4, 563, 1896.

Whiteman, C. D.: Mountain Meteorology: Fundamentals and Applications, Oxford University Press, New York, Oxford, 355 pp., 2000.

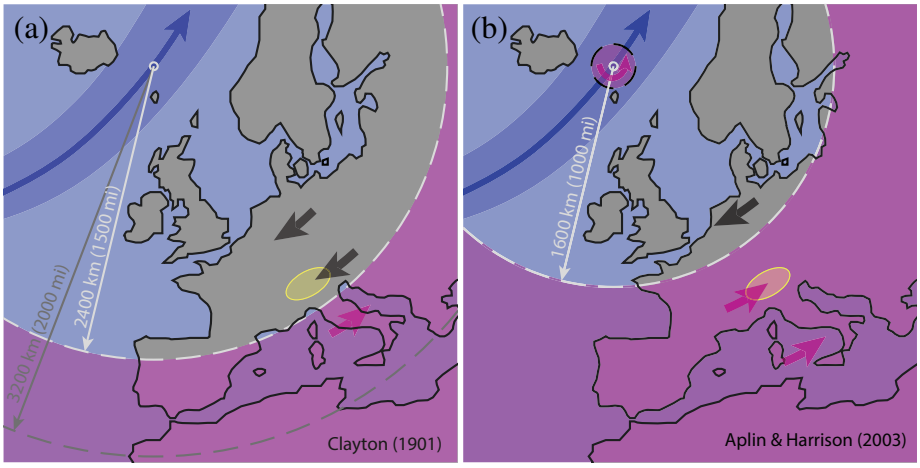

Figure 1. Theoretical effects of penumbral shading on wind direction. Wind directions around the center of the umbra (east of Iceland) according to the theory of Clayton (1901) (left) and Aplin and Harrison (2003) (right), schematically drawn for the time of maximum occultation over the Swiss Alps (yellow area). The eclipse trajectory is shown with a blue arrow, and the umbral path (100% occultation) is shown with a blueish band. The schematic shows the time of greatest eclipse with its center indicated by a gray circle.

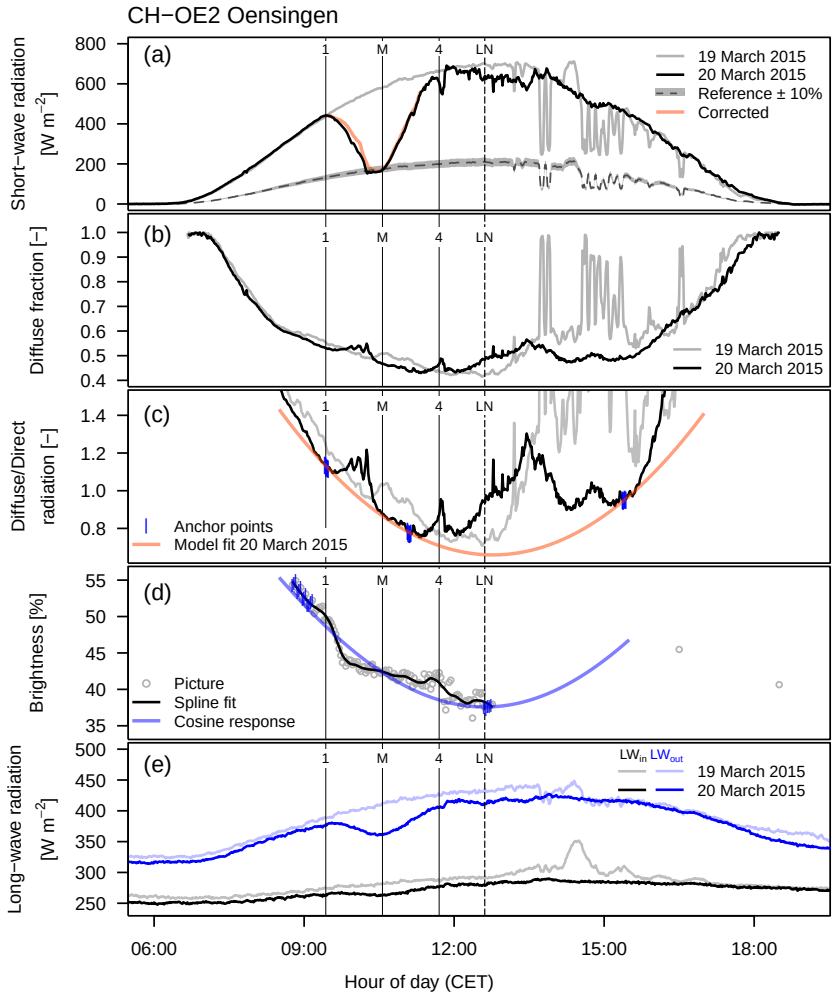

Figure 2. Radiation effects at the CH-OE2 Swiss FluxNet site. (a) Incoming short-wave radiation, (b) fraction of diffuse radiation, (c) ratio between diffuse and direct radiation, (d) evolution of brightness of the vegetation during the eclipse, and (e) long-wave radiation components. The four vertical lines indicate first contact (1), maximum occultation (M), last contact (4), and local noon (LN). Bold lines show the conditions during the day of the eclipse (black or darker color) in comparison with the preceding day (brighter color). The dashed reference curve in (a) is the measurement from 19 March 2015 multiplied by 0.6996, the theoretical maximum occultation at the site ($\pm$ 10% shown with a gray band). The fraction of diffuse radiation in (b) was measured with a quantum sensor measuring diffuse photosynthetic photon flux density (PPFD, 400–700 nm wavelength) in relation to total PPFD. The red model curve in (c) shows an empirical parabolic fit to the three periods with blue data points to obtain a reference for the correction of (a) for cloud passage during the eclipse (red line in (a)). The assumption made here is that the ratio of diffuse to direct PPFD is valid also for the entire wavelength spectrum of short-wave radiation shown in (a). During the penumbral shading phase, the phenological camera recorded images every 2 minutes, from which relative surface brightness was computed in the footprint area of the radiation measurements (gray symbols in (d)). The local polynomial regression fit (black line in (d)) shows a marked decrease in brightness after first contact in comparison to the theoretical cosine response (blue line in (d), anchored at the pictures marked with vertical blue bars), followed by an almost constant brightness during the occultation phase. LW_{in} and LW_{out} in (e) are incoming and outgoing long-wave radiation, respectively.

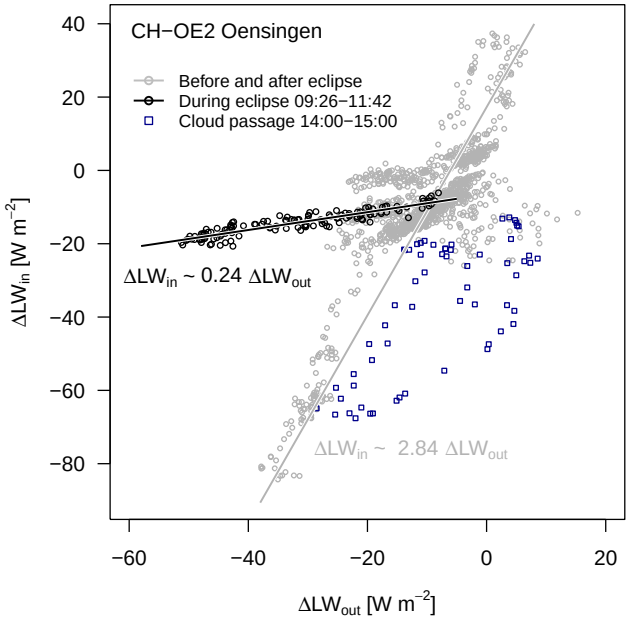

Figure 3. Long-wave back radiation effect during the eclipse (black symbols and regression line) in comparison to conditions before and after the eclipse (gray symbols and regression line). The differences ΔLW between 1-minute averages from the day before the eclipse and the same time during the day of the eclipse are shown (ΔLW_{in} in relation to ΔLW_{out} using the regression approach $\Delta LW_x = LW_x(20\text{ March}) - LW_x(19\text{ March})$ with x representing index $_{\text{in}}$ or $_{\text{out}}$). Measurements made during a period with cloud passage on 19 March 2015 (blue symbols) were excluded from analysis.

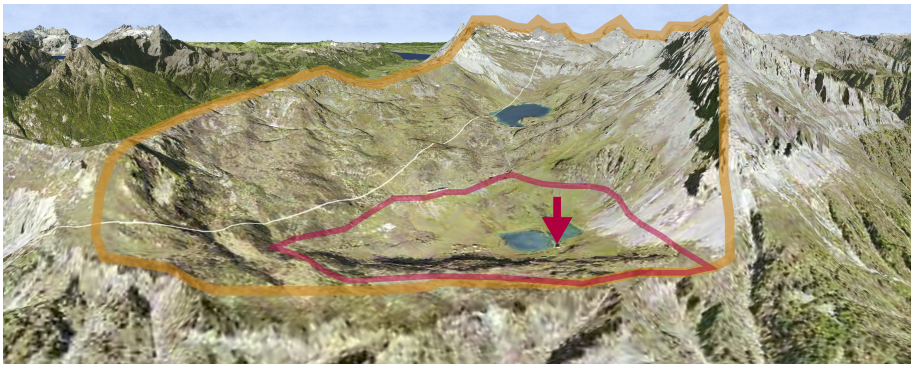

Figure 4. Oblique view of the surroundings of the Sorniot–Lac Inférieur de Fully weather station. The red arrow marks the location of the station, the red line marks the drainage area up to the lowest pass, and the orange line marks the full drainage area. The area was completely covered with snow and the lake was frozen during the eclipse. Imagery from Atlas of Switzerland V3 (Hurni, 2010), © 2016 swisstopo (JD100042).

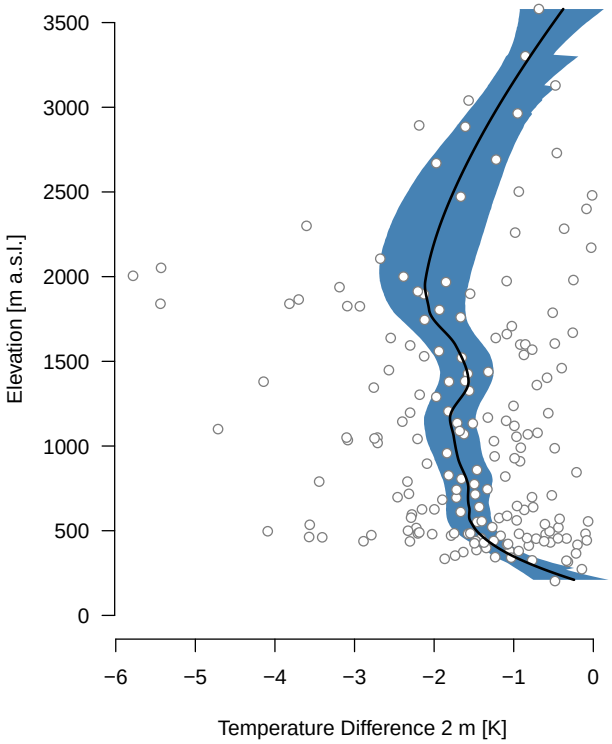

Figure 5. Temperature reduction maximum during the solar eclipse at 184 weather stations in Switzerland and Liechtenstein (open circles) that record 10-minute averages. The elevation profile (bold line showing the moving mean over a 350 m elevational window, equal to 10% of the entire elevation range) and its 95% confidence interval (blue band) were estimated using nonparametric bootstrapping.

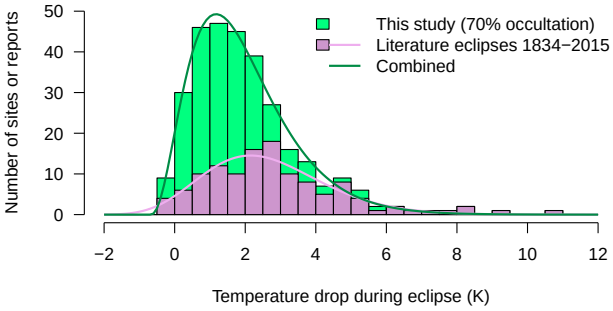

Figure 6. Histogram of temperature reduction at all sites included in this study and those reported in the literature. The stacked bars show number of sites of this study (green bars) on top of those for literature reports (violet bars). The solid lines show the best fit of the scaled probability distributions (Eq. 4, Table 2) of values reported in the literature (violet line) and the combination of literature data with values reported in this study (dark green line).

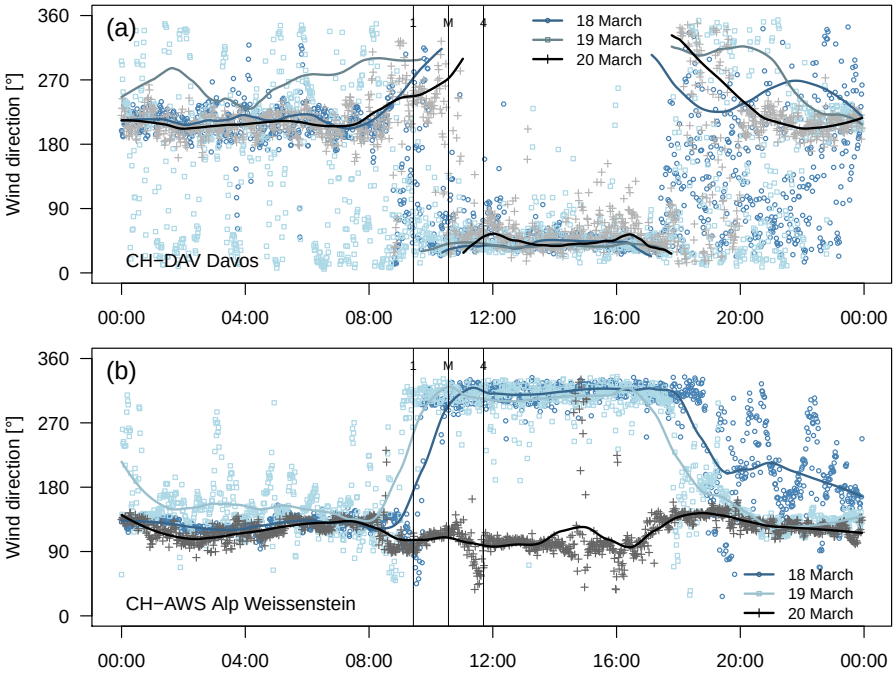

Figure 7. Wind direction as a function of time (a) at CH-DAV and (b) at CH-AWS on 18, 19 and 20 March, showing a delayed wind direction reversal at CH-DAV on 20 March (a), and a suppression of the typical wind reversal at CH-AWS on 20 March (b) determined from 1-minute average data. The bold lines are local polynomial regression (loess) fits.

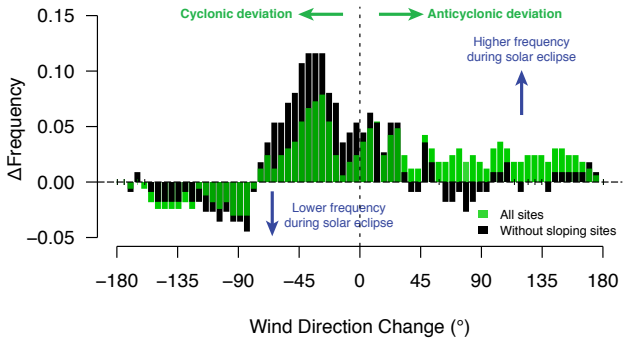

Figure 8. Deviation of wind direction changes (range –180° to 180°) during the eclipse expressed as ΔFrequency with respect to a random uniform distribution. The wind direction change is the difference between the first half of the eclipse in comparison with the corresponding time period on 19 March.

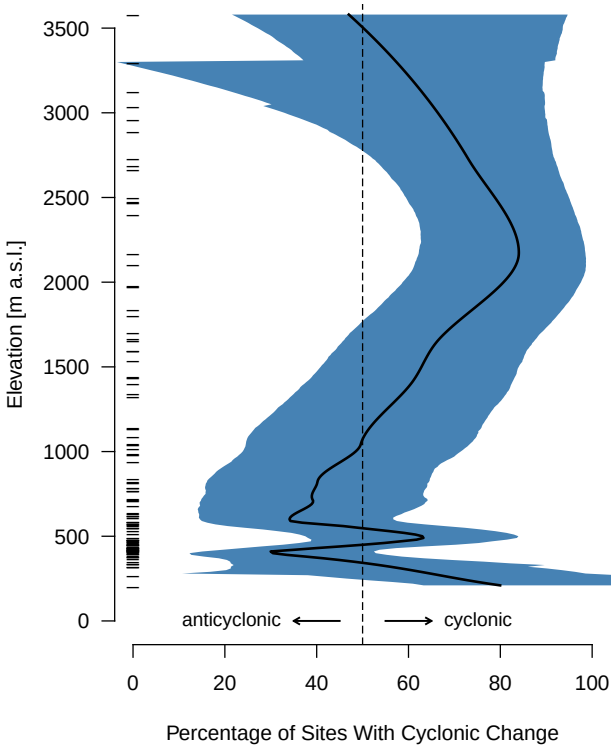

Figure 9. Elevation dependence of cyclonic and anticyclonic influences during penumbral shading. Using MeteoSwiss sites the percentage of sites showing cyclonic or anticyclonic effects was determined and elevational best estimates (bold line) and uncertainty of the estimate (90% confidence interval in blue) were estimated using nonparametric bootstrapping. The vertical dashed line at 50% indicates the insignificant random outcome. Each horizontal mark near the elevation axis represents one weather station.

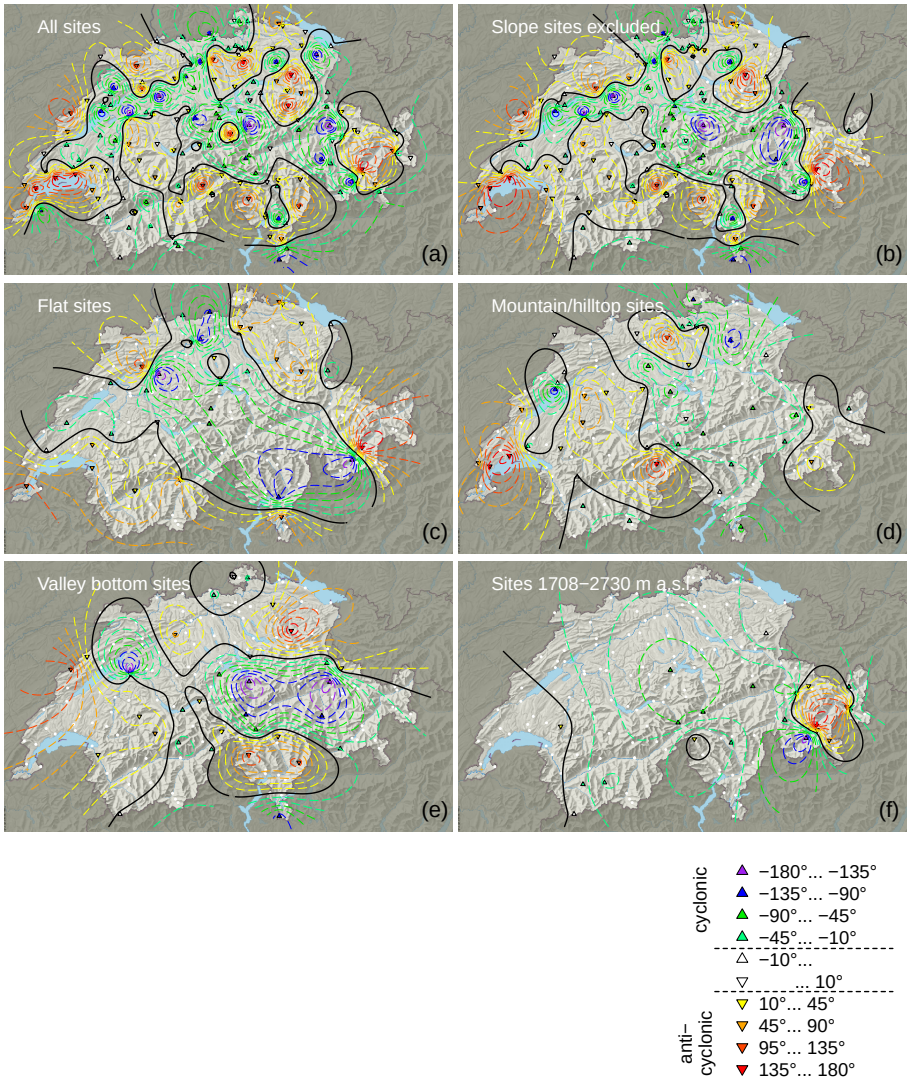

Figure 10. Spatial distribution of wind direction changes over Switzerland during the 20 March 2015 eclipse. Yellowish to reddish colors indicate anticyclonic rotation, while greenish to bluish colors indicate cyclonic rotation. The bold and broken isolines show lines of equal rotation angle at 20° intervals. The bold line separates areas with cyclonic from anticyclonic wind direction changes. Base map from Atlas of Switzerland V3 (Hurni, 2010), © 2016 swisstopo (JD100042).

Table 1. Compilation of literature reports on temperature drops during maximum occultation of the eclipse since 1834. Most reports are from total or annular eclipses, but a few studies also report values from partial eclipses or partial occultation at a given locality. More observations are tabulated in Aplin et al. (2016), but not all these reports allow the calculation of the temperature drop.

Date	Location | Additional Information	Temperature Drop	Reference
1834-11-30	Boston, Mass., USA	0.3 K	Anonymous (1834)
1896-08-09	Vadsö, Norway (70°04′ N)	1.0–1.6 K	Mill (1896)
1896-08-09	Vadsö, Norway (70°04′ N)	3.1 K	Ward (1896)
1905-08-30	Burgos	8.3 K	Reynolds (1937)
1918-06-08	Goldendale, Washington, USA	3.6 K	Anderson (1999)
1921-04-08	Bexley Heath	1.1 K	Bilham (1921)
1921-04-08	Bristol	4.2 K	Bilham (1921)
1921-04-08	Nottingham (Lenton Fields)	3.0 K	Bilham (1921)
1921-04-08	Prestou (Hoghton)	1.7 K	Bilham (1921)
1927-06-29	Bangor, UK	0.5 K	Owen and Jones (1927)
1927-06-29	English eclipse, cloudy	nothing remarkable	Reynolds (1937)
1927-06-29	Southport	0.5 K	Ashworth (1927)
1932-08-31	Canadian eclipse, cloudy	very small fall	Reynolds (1937)
1936-06-19	Chios	1 K	Reynolds (1937)
1936-06-19	Omsk	5 K	Reynolds (1937)
1936-06-19	on steam ship Strathaird	1.5 K	Reynolds (1937)
1936-06-19	Portugal	2.7–3.3 K	Reynolds (1937)
1936-12-13	New Plymouth, New Zealand	4.2 K	Hayes (1937)
1970-03-07	Lee, Florida, USA	3.2 K	Anderson et al. (1972)
1973-06-30	Chinguetti, Mauritania	3.5 K	Anderson and Keefer (1975)
1973-06-30	Chinguetti, Mauritania	2.5 K	Anderson and Keefer (1975)
1973-06-30	Chinguetti, Mauritania	2.5 K	Anderson and Keefer (1975)
1979-02-26	Hecla, Manitoba, Canada	2.0 K	Anderson (1999)
1984-05-30	'in Georgia'	7.8 K	Menke (1988)
1988-03-18	Ship, coast of Karimata island	2.2 K	Menke (1988)
1991-07-11	Agriculture/golf, wet fraction 1.00, albedo 0.20–0.25	1.40 K	Brazel et al. (1993)
1991-07-11	Costa Rica	no info	Fernández et al. (1993b)
1991-07-11	Costa Rica, Damas	4.7 K	Fernández et al. (1993a)
1991-07-11	Costa Rica, Fabio Baudrit Experimental Station	5.5 K	Fernández et al. (1993a)
1991-07-11	Costa Rica, Liberia, Alajuela and Palmar Sur	3.0–3.5 K	Fernández et al. (1993a)
1991-07-11	Costa Rica, Limón	3.0 K	Fernández et al. (1993a)
1991-07-11	Costa Rica, Puntarenas	2.7 K	Fernández et al. (1993a)
1991-07-11	Costa Rica, Santa Cruz and Filadelfia	2.0–2.5 K	Fernández et al. (1993a)
1991-07-11	Costa Rica, Tárcoles	8.5 K	Fernández et al. (1993a)

Date	Where | Additional Information	Temperature Drop	Reference
1991-07-11	Desert, wet fraction 0.00, albedo 0.27	2.65 K	Brazel et al. (1993)
1991-07-11	Fresno, California, USA, cotton field	ca. 4.5 K	Mauder et al. (2007)
1991-07-11	Industrial/airport, wet fraction 0.07, albedo 0.1	1.38 K	Brazel et al. (1993)
1991-07-11	Residential/commercial, wet fraction 0.47, albedo 0.20–0.25	1.93 K	Brazel et al. (1993)
1994-05-10	Ames, IA, USA	2.3 K	Segal et al. (1996)
1994-05-10	Boulder, CO, USA	2.2 K	Segal et al. (1996)
1994-05-10	Chicago, IL, USA	6.1 K	Segal et al. (1996)
1994-05-10	Estes Park, CO, USA	3.6 K	Segal et al. (1996)
1994-05-10	Ft. Collins, CO, USA	2.2 K	Segal et al. (1996)
1994-05-10	Keenesburg, CO, USA	3.0 K	Segal et al. (1996)
1994-05-10	Lakewood, CO, USA	2.7 K	Segal et al. (1996)
1994-05-10	Lamberton, MN, USA	3.1 K	Segal et al. (1996)
1994-05-10	Longmont, CO, USA	2.8 K	Segal et al. (1996)
1994-05-10	Loveland, CO, USA	3.3 K	Segal et al. (1996)
1994-05-10	Morris, MN, USA	2.3 K	Segal et al. (1996)
1994-05-10	Norman, OK, USA	3.6 K	Segal et al. (1996)
1994-05-10	Nowata, Oklahoma, USA	3.0 K	Anderson (1999)
1994-05-10	Nunn, CO, USA	1.9 K	Segal et al. (1996)
1994-05-10	Rollinsville, CO, USA	2.3 K	Segal et al. (1996)
1994-05-10	Sedalia, MO, USA	4.2 K	Segal et al. (1996)
1994-05-10	Springfield, IL, USA	6.1 K	Segal et al. (1996)
1994-05-10	St. Paul, MN, USA	1.5 K	Segal et al. (1996)
1994-05-10	Waseca, MN, USA	3.7 K	Segal et al. (1996)
1994-05-10	White Sands, New Mexico	5.5 K	Anderson (1999)
1994-05-10	White Sands, New Mexico	0.4 K	Anderson (1999)
1994-11-03	Coronel Oviedo, Paraguay	3.3 K	Fernández et al. (1996)
1995-10-24	Neem ka Thana, India	3 K	Jain et al. (1997)
1995-10-24	New Delhi, India	1.5 K	Jain et al. (1997)
1995-10-24	New Delhi, India	6–8 K	Jain et al. (1997)
1995-10-25	Hyderabad, India	9–10 K	Dutta et al. (1999)
1998-02-26	Sinamaica, Venezuela	5 K	Nufer and Gfeller (1998)
1999-08-11	Akola, Central India	1–2 K	Dolas et al. (2002)
1999-08-11	Kharkiv, Ukraine, max. occultation 0.73	7.3 K	Chernogor (2008)
1999-08-11	Modeling study, Central Europe	average 3.5 K	Gross and Hense (1999)
1999-08-11	Modeling study, Central Europe	peak up to 5 K	Gross and Hense (1999)
1999-08-11	Silsoe, Bedfordshire, UK, soil temperature at 10 mm depth	1.6 K	Leeds-Harrison et al. (2000)
1999-08-11	Silsoe, Bedfordshire, UK, under grass temperature	0.5 K	Leeds-Harrison et al. (2000)

Date	Where | Additional Information	Temperature Drop	Reference
1999-08-11	Southern UK	up to 3 K	Gray and Harrison (2012)
1999-08-11	Szczawnica, Poland	11 K	Szalowski (2002)
2001-06-21	Lusaka, Zambia	5.38 ± 0.04 K	Penaloza-Murillo and Pasachoff (2015)
2003-05-31	Kharkiv, Ukraine, max. occultation 0.64	2.1 K	Chernogor (2008)
2005-10-03	Kharkiv, Ukraine, max. occultation 0.24	1.3 K	Chernogor (2008)
2006-03-29	central Greece	2.7 K	Nymphas et al. (2009)
2006-03-29	Finokalia, Greece	2.3 K	Founda et al. (2007)
2006-03-29	Ibadan, Nigeria, 1 m	1.6 K	Nymphas et al. (2009)
2006-03-29	Ibadan, Nigeria, 12 m	0.8 K	Nymphas et al. (2009)
2006-03-29	Ibadan, Nigeria, 6 m	1 K	Nymphas et al. (2009)
2006-03-29	Kastelorizo, Greece	2.3 K	Founda et al. (2007)
2006-03-29	Kharkiv, Ukraine, max. occultation 0.77	2.3 K	Chernogor (2008)
2006-03-29	Kislovodsk, Russia	3 K	Gorchakov et al. (2008)
2006-03-29	Kislovodsk, Russia, 600 m a.s.l.	2 K	Gorchakov et al. (2007)
2006-03-29	Kislovodsk, Russia, surface atmospheric layer	3.4 ± 0.5 K	Gorchakov et al. (2007)
2006-03-29	Manavgat, Turkey	5 K	Stoev et al. (2008)
2006-03-29	Markopoulo (Athens), Greece	2.7 K	Founda et al. (2007)
2006-03-29	northern Greece	3.9 K	Nymphas et al. (2009)
2006-03-29	Palini (Athens), Greece	1.6 K	Founda et al. (2007)
2006-03-29	Penteli (Athens), Greece	2.7 K	Founda et al. (2007)
2006-03-29	Side, Turkey	5 K	Pleijel (2009)
2006-03-29	southern Greece	2.3 K	Nymphas et al. (2009)
2006-03-29	Thessaloniki, Greece	3.9 K	Founda et al. (2007)
2006-03-29	Thission (Athens), Greece	2.6 K	Founda et al. (2007)
2006-03-29	Athens, Greece	0.7 K	Tzanis et al. (2008)
2006-03-29	Ibadan, Nigeria	2.2 K	Economou et al. (2008)
2008-08-01	Svalbard, Norway	0.3–1.5 K	Sjöblom (2010)
2010-01-15	Gadanki, India, –0.10 m	3.0 K	Venkat Ratnam et al. (2010)
2010-01-15	Gadanki, India, –0.20 m	1.3 K	Venkat Ratnam et al. (2010)
2010-01-15	Gadanki, India, 0.00 m	5.4 K	Venkat Ratnam et al. (2010)
2010-01-15	Gadanki, India, 0.05 m	5.0 K	Venkat Ratnam et al. (2010)
2010-01-15	Gadanki, India, 12 m	2.5 K	Venkat Ratnam et al. (2010)
2010-01-15	Gadanki, India, 4 m	5 K	Venkat Ratnam et al. (2010)
2010-01-15	Gadanki, India, 8 m	3 K	Venkat Ratnam et al. (2010)
2010-01-15	Gadanki, India, surface	5.8 K	Venkat Ratnam et al. (2010)

Date	Where | Additional Information	Temperature Drop	Reference
2010-01-15	Kanyakumari, India	4 K	Murthy et al. (2013)
2010-01-15	Ramanathapuram, India	1 K	Murthy et al. (2013)
2010-01-15	Thiruvananthapuram, India	1.2 K	Bala Subrahamanyam and Anurose (2011)
2010-01-15	Thiruvananthapuram, India, over cassava	4 K	Murthy et al. (2013)
2010-01-15	Thrissur, India	2 K	Murthy et al. (2013)
2010-01-15	Thumba, India	2 K	Murthy et al. (2013)
2010-01-15	Thumba, India	1.2 K	Bala Subrahamanyam et al. (2012)
2010-01-15	Tirunelveli, India	3.2 K	Murthy et al. (2013)
2015-03-20	Mainland UK, maximum drop (of 266 sites)	4.23 K	Clark (2016)
2015-03-20	Mainland UK, median drop (of 266 sites)	1.02 K	Clark (2016)
2015-03-20	Mainland UK, minimum drop (of 266 sites)	0.03 K	Clark (2016)
2015-03-20	Mainland UK, mean drop (of 76 sites)	0.83 ± 0.63 K	Hanna et al. (2016)
2015-03-20	Mainland UK, mean drop, clear sky (14 sites)	0.91 ± 0.78 K	Hanna et al. (2016)
2015-03-20	Mainland UK, mean drop, cloudy sky (16 sites)	0.31 ± 0.40 K	Hanna et al. (2016)
2015-03-20	Svalbard, Norway	0.3–1.5 K	Pasachoff et al. (2016)
2015-03-20	Switzerland, 184 stations	1.5 K	*This study*
2015-03-20	Sorniot–Lac Inférier (Switzerland, most extreme drop)	5.8 K	*This study*

Table 2. Fitting parameters of gamma distribution (Eq. 4) fitted to empirical histograms of temperature drops ΔT during the eclipses and mean ΔT. All values are best estimates $\pm$ standard error of the estimate. Values in italics indicate that the parameter estimates were not significantly different from zero ($p > 0.05$).

	Offset (K)	Shape	Scale	mean ΔT (K)
This study	-1.1 ± 0.3	6.6 ± 1.9	0.4 ± 0.1	1.5 ± 1.0
Literature data	*–3.5 ± 3.1*	*12.8 ± 13.1*	*0.5 ± 0.3*	2.6 ± 1.7
Combined	-0.7 ± 0.1	3.4 ± 0.4	0.8 ± 0.1	1.9 ± 1.4

Table 3. Empirical probabilities Pr($\leq \Delta$T) to relate a future temperature drop during an eclipse to values previously published in the literature and in this paper. Bold figures are above the median, and figures in italics are below the 10% percentile of the empirical probability distribution. The sign convention uses positive ΔT if temperature gets colder during the occulation phase.

ΔT (K)	All	Literature	This study
11.0	*<0.001*	*<0.001*	*<0.001*
10.5	*0.003*	*0.008*	*<0.001*
10.0	*0.003*	*0.008*	*<0.001*
9.5	*0.003*	*0.008*	*<0.001*
9.0	*0.007*	0.017	*<0.001*
8.5	*0.007*	0.017	*<0.001*
8.0	0.013	0.033	*<0.001*
7.5	0.016	0.041	*<0.001*
7.0	0.020	0.050	*<0.001*
6.5	0.023	0.058	*<0.001*
6.0	0.030	0.074	*<0.001*
5.5	0.036	0.083	*0.005*
5.0	0.056	0.116	0.016
4.5	0.085	0.182	0.022
4.0	0.108	0.223	0.033
3.5	0.151	0.289	0.060
3.0	0.203	0.372	0.092
2.5	0.292	**0.521**	0.141
2.0	0.420	**0.653**	0.266
1.5	**0.567**	**0.736**	0.457
1.0	**0.721**	**0.835**	**0.647**
0.5	**0.872**	**0.917**	**0.842**
0.0	**0.970**	**0.967**	**0.973**
–0.5	>**0.999**	>**0.999**	>**0.999**
–1.0	>**0.999**	>**0.999**	>**0.999**
–1.5	>**0.999**	>**0.999**	>**0.999**
–2.0	>**0.999**	>**0.999**	>**0.999**